IJPPR
INTERNATIONAL JOURNAL OF PHARMACY & PHARMACEUTICAL RESEARCH
An official Publication of Human Journals
ISSN 2349-7203
HUMAN

Human Journals
Research Article
October 2018 Vol.:13, Issue:3

Insights into Characterization and Adsorptive Behaviour of Zeolitized Brick in Water toward Cadmium (A Very Toxic Heavy Metal to Humans)

IJPPR
INTERNATIONAL JOURNAL OF PHARMACY & PHARMACEUTICAL RESEARCH
An official Publication of Human Journals
ISSN 2349-7203
HUMAN

Nicole Poumaye[1,2], Oscar Allahdin[1,2], Michel Wartel[2], Abdel Boughriet[2*]

1. Chaire Unesco « Sur la gestion de l'eau », Laboratoire Hydrosciences Lavoisier, Université de Bangui, Faculté des Sciences, B.P. 908, République Centrafricaine.

2. Université Lille1, Laboratoire LASIR (UMR CNRS 8516), Equipe Physico-chimie de l'Environnement. Bât. C8 2ème étage, 59655 Villeneuve d'Ascq cedex, France.

Submission: 20 September 2018
Accepted: 27 September 2018
Published: 30 October 2018

Keywords: brick; metakaolinite; alkaline activation; sodic aluminosilicates; cadmium(II); adsorption. Nicole Poumaye[1,2], Oscar Allahdin[1,2], Michel Wartel[2], Abdel Boughriet[2*].

ABSTRACT

The material studied here is a brick mainly composed of sand and metakaolinite. Its alkali treatment with sodium hydroxide was carried out at fixed reaction time and temperature. Chemical, mineralogical and structural composition of synthesized products was determined using X-ray diffraction, ICP-AES, ESEM/EDS, and vibrational spectroscopies (FTIR and micro-Raman). Analytical and spectroscopic data permitted us to evidence the occurrence of zeolites (in Na-forms). Particularly, they revealed that the atomic ratio Si/Al in these aluminosilicates was close to 1 and the resulting 'negative charges' deficit was compensated by the presence of Na^+ ions The atomic ratio Na/Al ratios was < 1, suggesting that other cations such as K^+, Ca^{2+} and/or Mg^{2+} (detected by ESEM/EDS) contributed as well to assure the electric charges balance of these zeolitic networks. Adsorptive behaviour of alkali brick toward cadmium (as a model toxic heavy metal) in water was tested in fixed-bed column, and results showed relevant adsorption capacities when compared to those obtained with coated sands, natural zeolites and coated/modified zeolites.

HUMAN JOURNALS
www.ijppr.humanjournals.com

1. INTRODUCTION

The presence of intensive human activities and industries has resulted in heavy metal contamination in urban soils and immediate aquatic systems. As a consequence, water sources in developing countries contain high amounts of various ions and heavy metals which were often above limit prescribed by the World Health Organization (WHO). The majority of these waters need therefore to be treated before using them as drinking water and even for domestic applications. Among these heavy metal pollutants, cadmium is considered as a very toxic element for human health, even in small amounts. Thus, WHO guideline for drinking water quality recommends for cadmium a value not exceeding 0.003mg.L^{-1} [1]. Longtime occupational exposure to Cd may contribute to the developing of diseases such as: kidney failure [2]; liver disease [3]; osteoporosis [4]; neuro-degeneration [5]; diabetes mellitus [6]; cardiovascular disorders [7]; and cancer [8]. Due to high health risks, cadmium was chosen in the present study as a "model metal contaminant" in order to test zeolitized brick as an adsorbent material for water treatment at low cost in rural regions of developing countries.

Zeolites (as alumino-silicates) had been found to be attractive compounds in numerous industrial and environmental applications due to their particular surface characteristics, ***i.e.***: porous alumino-silicate framework, large surface area, channels, cages or cavities in which sorption and diffusion of ions and molecules can occur [9, 10]. If negative charges exist in the zeolites, the charge imbalance is offset by the incorporation of extra-framework cations (such as: Na^+, K^+ and/or Ca^{2+} ions) into their structure. Potential industrial applications of zeolites in specific chemical processes had often necessitated an adequate crystallization with particular structural/morphological characteristics. Owing to these properties, zeolites had been widely studied in catalysis [11-15], gas separations and catalysis [16], and particularly, they had been intensively used in petrochemical industry as molecular sieve and/or catalytic materials in different reactions such as: (i) organic synthesis [17, 18] and gasoline manufacture and production [19, 20]. Moreover, zeolitic frameworks contain H_2O molecules and exchangeable cations that are associated with negatively charged sites. Thus, by employing zeolites as ions-exchangers, the existence of surface charges that generate electrostatic forces at the zeolite/water interface enables counter-ions (like alkaline or alkaline-earth cations) to be substituted by other cations. This explains why some zeolites had been found to be useful in environmental applications [21] and/or suitable for their use in detergents formulation [22, 23]. They were used as ions-exchangers in water treatment /

remediation: (i) for the softening of waters with high levels of hardness caused by calcium (Ca^{2+}) and magnesium (Mg^{2+}) [24, 25]; (ii) for the removals of toxic metals such as: Co(II), Cu(II), Zn(II), Ni(II), Cr(III), Cd(II) and Pb(II) [26-33]; and (iii) for water decontamination from radioactive elements such as Cs^{+} and Sr^{2+} [34-35].

Over the last decades, extensive research efforts have been focusing on finding low-cost clay minerals as starting materials for zeolites preparations. For instance, numerous studies had been devoted to the use of kaolinite as a zeolite precursor by exploring the well-known reactivity of its calcined form (metakaolinite) [36-39]. This alumino-silicate with a Si/Al atomic ratio of 1 was indeed recommended in the recent literature as a convenient starting material for the hydrothermal synthesis of zeolites with sodium hydroxide [40-42]. For instance, metakaolinite-derived zeolites were employed in the Fe(II) and Mn(II) removals from aqueous solutions. [39, 43].

Brick is made craftily in Bangui region (Central African Republic) from local soils that contains a high proportion of kaolinite (20-25 w%) in addition to sand (60-65 w%). The thermal treatment of these soils was performed in the temperature range of 600-750°C, and permitted the conversion of kaolinite ($Al_2O_3.2SiO_2.2H_2O$) into metakaolinite ($Al_2O_3.2SiO_2$). Recently, Bangui brick after its acid activation followed by an iron oxihydroxide coating, had been tested in our lab as a metals adsorbent. The resulting experimental data had revealed good adsorption capacities of this modified brick in the removal of heavy metals such as: Fe^{2+}, Pb^{2+}, Cd^{2+}, Cu^{2+} and Zn^{2+} from aqueous solutions [44-51]. And during our performed column experiments the presence of sand (60-65 wt%) in brick pellets contributed to assure a good permeability and to facilitate the flow of water through brick beds. It is interesting to note that other types of bricks had also been utilized as low−cost adsorbents for removing metals like: Hg(II) [52]; Zn(II) [53]; Cr(VI) [54]; both Cr(VI) and Ni(II) [55]; or Ni(II) alone [56].

In the present study, Bangui brick was treated under alkali conditions in the aim to transform brick metakaolinite into zeolites. The synthesized materials were characterized by ICP-AES analysis, X-ray diffraction (XRD), vibrational spectroscopies (FTIR and micro-Raman), and Environmental Scanning Electron Microscopy (ESEM) coupled with Energy Dispersive X-ray Spectroscopy (EDS). Column experiments were afterwards conducted in the lab in order to test the efficiency of this new material for the removal of cadmium(II) from aqueous solutions.

2. MATERIALS AND METHODS

2.1. Adsorbents preparation

The raw brick used in this study was obtained from Bangui region in the Central African Republic. Previously [26], X-ray diffraction and chemical analysis were performed on this material in order to identify mineral compounds and to assess their proportions: mainly 60-65 wt % quartz (SiO_2) and 20-25 wt % metakaolinite ($2SiO_2.Al_2O_3$); and to a lesser extent: 4-5 wt % illite; ≤ 4 wt % iron oxides / hydroxides; and ≤ 3 wt % feldspar + mica + biotite. Before use as an adsorbent, several physical/chemical treatments were carried out on the raw brick. First, it was broken into grains and sieved with sizes ranging from 0.7 to 1.0 mm. Second, the resulting particles were leached with Milli-Q water at room temperature for 24 hours. Third, brick pellets were treated in our laboratory under the following alkali conditions: : 10 g of Bangui brick reacted in 40 mL of a NaOH solution with [NaOH] varying from 0.1 to 1.5mol/L at the different reaction temperatures: 50, 70 and 90°C, and for a constant reaction time of six days. The recovered grains were afterwards rinsed several times with MilliQ water and dried at 90°C for 24 hours.

2.2. Chemicals

All chemicals employed in the experiments were analytical grades. Sodium hydroxide and nitric acid were supplied by DISLAB (France). The $Cd(NO_3)_2.4H_2O$ salt was purchased from Prolabo.

2.3. ICP-AES analyses

All chemical attacks of brick materials were made with 2M nitric acid at 90°C for 2 hours. The recovered solutions were analyzed for metal contents using ICP-AES (Inductively Coupled Plasma – Atomic Emission Spectroscopy; model Varian Pro Axial View).

2.4. Electron Microscopy analysis

Micrographies of representative specimens of alkali brick were recorded using an environmental scanning electron microscope (ESEM, Quanta 200 FEI). Elemental analysis was performed using ESEM/EDS (ESEM, model: QUANTA–200–FEI, equipped with an Energy Dispersive X-Ray Spectrometer EDS X flash 3001 and monitored by QUANTA–400 software elaborated by Bruker). EDS measurements were carried out at 20 kV at low vacuum

(1.00 Torr) and the maximum pulse throughput was 20 kcps. Different surface areas ranging from 0.5 to 3.5 mm² were targeted on alkali-brick grains and examined by ESEM/EDS. For that, a narrow beam scanned selected areas of brick pellets for chemical analysis. Atomic quantifications and mathematical treatments were undertaken using QUANTA-400 software in order to determine the averaged elemental composition of the surface brick and to detect chemical/elemental variabilities.

2.5. Fixed-bed column experiments

Continuous flow adsorption experiments were conducted in a fixed-bed glass column with an inner diameter of 12.5 mm, a height of 25 cm, and a 160-250 µm porosity sintered-pyrex disk at its bottom in order to prevent any loss of material. A bed depth of 6.7-6.9 cm (5.0029-5.0102 g) was investigated at a constant flow rate of 2.5mL.min^{-1}. Before being used in the experiments, at least 500 mL of Milli-Q water were passed through the column. The schematic diagram of the fixed-bed column reactor used is illustrated in reference 51. The initial concentration of metal cation (Cd^{2+}) in the influent was 54 mg/L (or 4.85x10^{-4} mol.L^{-1}). The influent pH ranged from 4.9 to 5.0. The divalent - metal solution was pumped through the column at a desired flow rate by means of a peristaltic pump (LaboModerne France Type KD1170) in an up-flow mode. During this column experiment, the effluent pH was measured continuously by means of a pH meter which was connected to a computer, as described in Fig. 1; and effluent samples exiting the bottom of the column were collected at different time intervals and analyzed for metal contents using ICP-AES. Flow to the column continued until the effluent metal concentration at time t (C_t) reached the influent metal concentration (C_0): $C_t/C_0 \approx 0.99$. Performance of the packed bed was described in the present work using the concept of the breakthrough curve. Breakthrough profiles yield two important time: (i) the breakthrough time, noted $t_{b.}$, when $C_t = 0.05C_o$; and (ii) the exhaustion time, noted $t_{exh.}$, when $C_t = 0.95C_o$.

3. RESULTS

3.1. Optimization of the synthesis

It was previously found that under alkali conditions chemical transformations of metakaolinite (which is present in Bangui brick at proportions ranging from 20 to 25 %) resulted in negatively-charged structures of alumino-silicate minerals as: >Si–O$^-$ and >Al–O$^-$ [57]. The appearance of negative sites in the framework is balanced by that of counter-ions

(Na^+ ions). During an adsorption process, monovalent cations (Na^+ ions) present at the brick surface can be substituted by divalent metal cations (Me^{2+}), and hence, can be released into the reaction medium. In this context, the global reaction can be written as follows (equation 1):

$$2(>S–O^- ---Na^+) + Me^{2+} \leftrightarrow (>S–O)_2Me + 2Na^+ \quad (1)$$

Where "$>S–O^-$---Na^+" represents an ion-pair at the water/brick interface. The occurrence of reaction (1) was evidenced by means of column experiments, as described in section 3.5. Under such an assumption, the quantity of sodium bound to the brick could, therefore, be considered as a key indicator of both the alkali-reaction course/extent and the number of reactive sites. For that purpose, brick pellets with size diameters ranging from 0.7 to 1.0 mm were treated in different alkaline solutions as described in the experimental section. The synthesized alkali - brick samples were afterwards attacked thoroughly in 2 $mol.L^{-1}$ HNO_3, and subsequently, ICP-AES analysis was performed on recovered solutions. The 3-D histogram shown in Fig. 1 represents the evolution of the total amount of sodium in the brick samples obtained after different NaOH treatments.

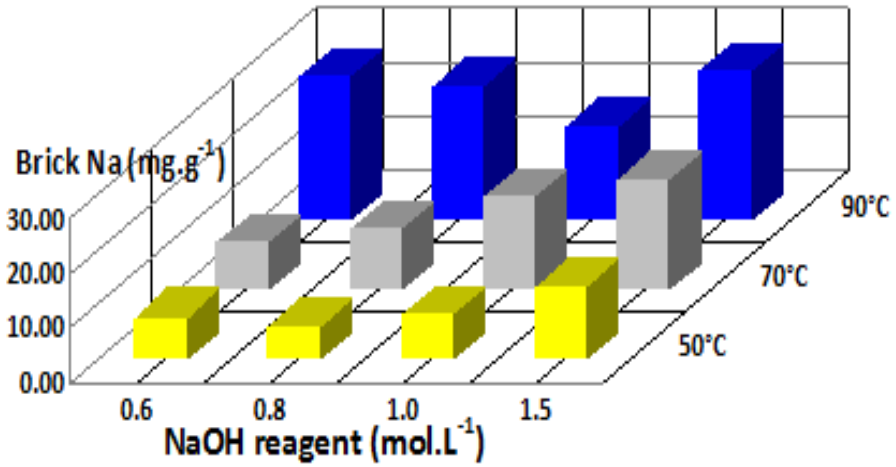

Figure 1: 3-D histogram showing the evolution of the total amount of sodium in the brick samples after different NaOH treatments according to the following procedure: 10 g of raw brick reacted in 40 mL of a NaOH solution with [NaOH] varying from 0.1 to 1.5 $mol.L^{-1}$ at different reaction temperatures: 50, 70 and 90°C, and for a constant reaction time of six days.

As can be seen in this figure, the quantity of brick - bound Na reached a maximum value when the synthesis was carried out in a 0.6mol.L^{-1}-NaOH solution and decreased when the NaOH - reagent concentration became > 0.8 mol.L^{-1}. This depletion might be due to a progressive degradation of the brick minerals under strong alkali conditions in accordance with ESEM images (see section 3.4).

At the end of the different performed syntheses, attempts of Raman and FTIR detection and identification of solutes like: silicate and aluminate and/or polymeric alumino-silicate complexes were made in recovered solutions (as observed previously with other clays and/or alumino-silicates in alkali media [58-62]. Unfortunately, none of these solutions had enough solutes to be reasonably detectable and, as a consequence, it had not been possible to evaluate the chemical stabilities of brick products generated under our alkali conditions by means of these vibrational techniques. In contrast, the use of the ICP-AES technique permitted us to detect and quantify the amounts of soluble silicon and aluminium released into the synthesis medium at the end of each alkali-reaction procedure (Fig. 2).

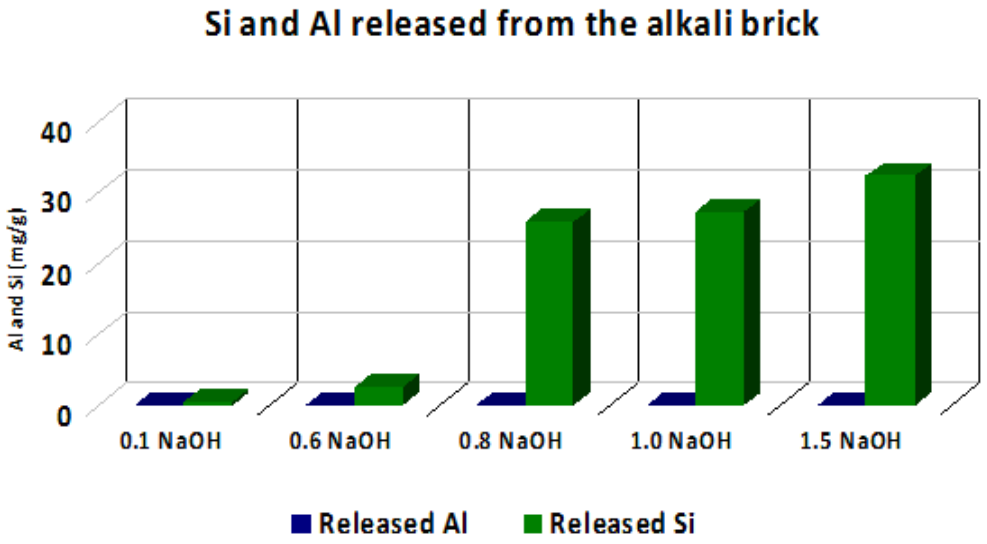

Figure 2: Amounts of soluble silicon and aluminium released into the synthesis medium at the end of each alkali-reaction procedure described as follows: 10 g of raw brick reacted in 40 mL of a NaOH solution with [NaOH] varying from 0.1 to 1.5 mol.L^{-1} at a fixed reaction temperature of 90°C, and for a constant reaction time of six days.

As can be seen in this figure, a significant increase of the Si concentration occurs when the [NaOH] concentration in the reaction medium becomes higher than 0.6mol/L. This might mean that a presumed chemical degradation of the brick took place under strong alkali

conditions, as suggested above in our discussions about Fig. 1. It is however worth noting that, as a result of such a brick decomposition, "solute" aluminate species were barely detected in the reaction solution (as shown in Fig.2) for two reasons: (i) the Si(0Al) atoms are more dissolved than the other Si(nAl) atoms (with n≠0) present in the zeolitic─brick framework [63]; and (ii) probably saturation/condensation and/or precipitation/adsorption of soluble Al compounds occur onto the remaining material, as suggested previously ([60, 63].

These investigations led us to focus our attention principally on products formed in 0.6 mol.L^{-1} and 0.8 mol.L^{-1} NaOH solutions at the temperature of 90°C and a reaction time of six days.

3.2. Mineralogical properties of NaOH - treated brick

In this article, framework type codes of zeolites are given in accordance with the Classification of the International Zeolite Association. Fig. 3 illustrates the XRD patterns of Bangui brick before and after subjecting to alkali treatment at the scanning Bragg angle (2θ) ranging from 10° to 60°.

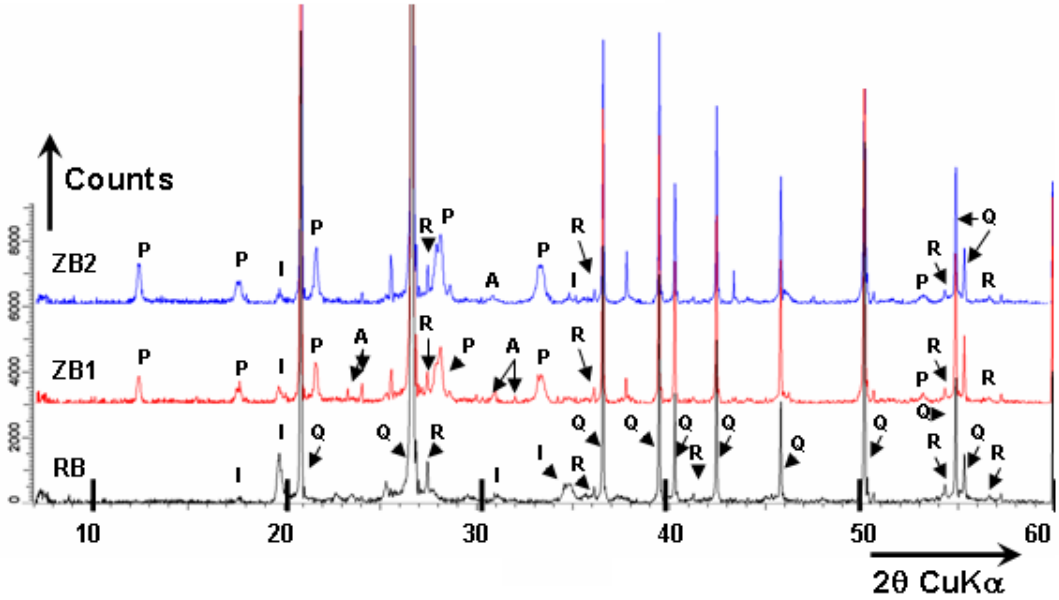

Figure 3: XRD patterns of raw brick before and after alkaline treatment at 90°C for 6 days (10g of raw brick treated in 40 mL of NaOH solution): RB, raw brick; ZB1, zeolitized brick obtained after treatment in a 0.6mol.L^{-1} NaOH solution; ZB2, zeolitized brick obtained after treatment in a 0.8mol.L^{-1} NaOH solution. *I, illite; Q, quartz; R, rutile; P, NaP zeolite; and A, NaA zeolite.*

In raw brick, quartz, illite and rutile were found to be the main crystalline phases. Quartz was identified on the basis of the following '2θ' reflection angle (the Miller indices, hkl, are given in the parenthesis): 20.9° (100); 26.6° (011); 36.5° (110); 39.5° (102); 40.3° (111); 42.4° (200); 45.8° (201); 50.2° (112); and 54.9° (022) [ICSD Collection Code: 89276]. Because of the smaller amounts of illite and rutile in the brick, these two minerals were recognized only on the basis of some of their intensive reflection angles: ***illite***: 17.9° (004), 19.8° (021), 31.1° (007), 34.3° (034), and 37.1° (117) [ICDD (International Centre for Diffraction data): 00-009-0343]; ***rutile***: 27.4° (110), 36.1° (101), 41.2° (111); 44.0° (210), 54.3° (211), and 56.6° (220) [ICSD Collection Code: 168140]. Normally, metakaolinite gives a broad featureless signal ([38,63] Heller-Kallai and Lapides, 2007a and b): its intensity maximum is measured at 2θ°(radiation $K_{\alpha 1}$Cu) ≈ 22° [64]. Unfortunately, metakaolinite was not detected in the X-ray diffractogram of raw brick because of the low content of this alumino-silicate mineral in Bangui brick (indeed, metakaolinite represents less than 25% of the total brick weight).

During the heating process of the brick at 90°C with sodium hydroxide, no significant difference between XRD patterns of the raw brick and the products was obtained after one day alkali treatment (not shown here). Noticeable crystalline transformation of the brick was observed only after three days alkali treatment (not shown here). After six days alkali treatment in a 0.6mol.L^{-1}─NaOH solution, the mineral composition of the brick changed significantly with the appearance of new peaks in the X-ray diffractogram in addition to those ascribed to quartz, illite and rutile. The XRD pattern of the recovered product indeed shows at least six main characteristic peaks at 2θ: 12.5°; 17.7°; 21.7°; 28.2°; 33.4°; and 53.2° [65] (see Fig. 3), confirming the formation of the NaP zeolite as the major new crystalline phase of the treated brick. Although the zeolitic material observed in NaOH─treated brick was predominantly NaP, the *Linde Type A* (LTA) zeolite was also identified in the X-ray diffractogram, but this crystalline phase was found to be a lower amount than that of NaP. LTA was recognized by the following '2θ' reflection angles: 22.8° (620); 24.0° (622); 30.0° (644 and 820); 30.8° (822 and 660); 31.7° (662); and 34.2° (664) [65] (see Fig. 3).

In order to study the effect of NaOH/brick ratio on zeolitization process, the basic treatment was afterwards conducted with a higher NaOH concentration (0.8 mol.L^{-1}) under the same temperature/reaction time conditions (***i.e.***, at 90°C and for six days). The XRD pattern of the recovered product, which is illustrated in Fig. 3, revealed that increasing the NaOH concentration from 0.6 mol.L^{-1} to 0.8 mol.L^{-1} favoured the formation of NaP crystals at the

expense of LTA ones. This observation suggested that, under our experimental conditions, LTA zeolite transformed into a more stable phase, NaP zeolite [40, 66]. Note that illite peaks began decreasing but still existed when the NaOH concentration increased from 0.6 to 0.8mol/L. These peaks decreases might be due to a partial alkali dissolution of illite, as pointed out previously [67, 68].

3.3. Vibrational spectroscopy analyses

3.3.1. FTIR spectroscopy

As shown in Fg. 4, the most intense band at around 1025 cm^{-1} observed for raw brick is due to internal Si–O(Al or Si) bonds vibrations that take place in aluminium- and silicon-oxygen bridge. Under the effects of NaOH concentration (0.6 and 0.8 $mol.L^{-1}$) and temperature (90°C) on the brick structure (for a synthesis time of six days), Infrared-red studies showed a slight shift of the band at 1025 cm^{-1} towards lower wave-numbers, at around 1000 cm^{-1} (Fig. 4). Comparable shifts were already observed for aluminosilicates present in slurry and fly ash, indicating zeolitization of these compounds to NaP zeolite (see [69] and references therein). The band shifting observed here suggested that, during the structural/crystalline modifications of the brick, the number of aluminium atoms in the tetrahedral positions increased when compared to that found in the raw material in agreement with ^{27}Al MAS NMR results (see section 3.4.3). The appearance of the band at about 1000 cm^{-1} is probably due to the asymmetric - stretch vibrations of internal Si─O or Al─O tetrahedra in the NaP framework [69, 70]. The band at around 950 cm^{-1} was often assigned to Si–OH bending vibrations and might be caused by formation of very small zeolitic crystals with extended external area and thereby imposing a greater number of terminating silanols [71].

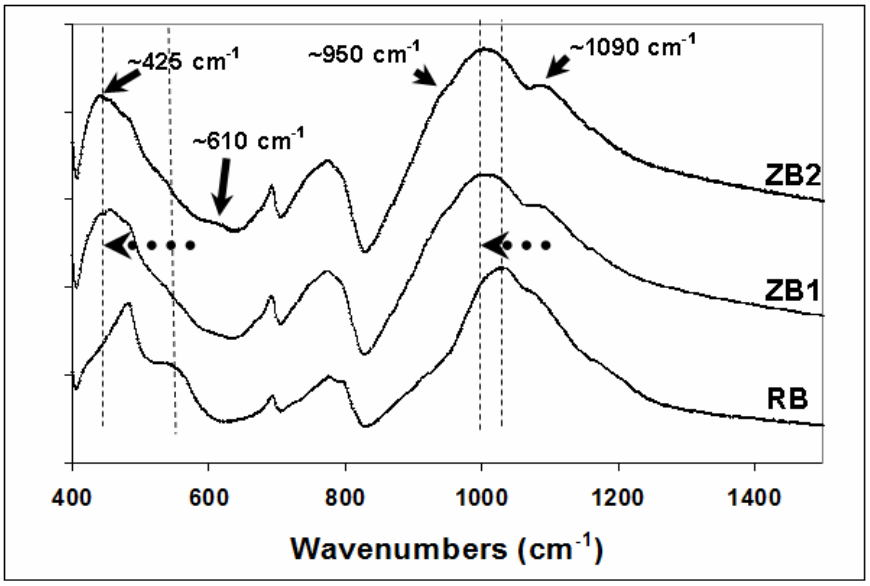

Figure 4: FTIR spectra observed for raw brick (RB) and zeolitized brick obtained after treatment in a 0.6 mol.L^{-1} NaOH solution (ZB1) and 0.8 mol.L^{-1} NaOH solution (ZB2) at 90°C for 6 days (10 g of raw brick were treated in 40 mL of NaOH solution).

The alkali treatment brought outbreaking of Si–O–Si bridges which led to the clear appearance of a band at 960 cm^{-1} (see Fig. 4), as a result of an increase of Si–O nonbridging terminal bonds in the brick structure [72]. The band at ~1090 cm^{-1} also appears clearer after the alkali treatment of the brick (Fig. 4): it can be assigned to internal Si–O(T) bonds vibrations occurring in Al- or Si-oxygen bridges [72]. As for the badly-resolved band(s) appearing at higher wave-numbers in the range of 1150-1165 cm^{-1}, it can be ascribed to asymmetric stretching vibrations [72].

The bands observed in the range of 500-800 cm^{-1} were difficult to assign because the FTIR spectra in this range are the superposition of the bands of both brick minerals (not transformed) and generated zeolites. However, it can be seen in Fig. 4 a weak band at about 610 cm^{-1}, which was detectable only for NaOH - treated brick and not for raw brick. This band should result from the occurrence of NaP zeolite in the modified brick ([69, 70, 72-75]. This band is attributable to the symmetric stretching vibrational mode of internal tetrahedron in the NaP zeolite [73, 76]. Furthermore, after alkali treatment it was observed two particular features in the spectral region considered (see Fig. 4): first, a shift of the bands of raw brick in the range of 450-550 cm^{-1} towards lower wave-numbers; and second, the appearance of new bands which are badly resolved and typical for sodium alumino-silicates [74, 77]. According these latter authors, the bands in the range of 400-600 cm^{-1} result from Al–O(H) and bending

deformation of Si(Al)–O. Similar FTIR bands were previously observed for NaP zeolite generated from starting materials like: (i) wastes from metallurgical industry containing Al_2O_3 and SiO_2 with Al_2O_3 /SiO_2 molar ratio ≅ 7.3 [75]; or (ii) kaolin [78]. Particularly, it can be noticed a band at the lower wave-numbers, ~425 cm^{-1} (see Fig. 4), that appears better under increasing alkali conditions, suggesting the formation of NaP zeolite in NaOH - treated material. The 425 cm^{-1} band would be due to internal vibrations of $(Si,Al)O_4$ tetrahedra in the brick framework, and would result from stretching and bending modes of the T–O (T = Si or Al) units [69, 79].

3.3.2. Micro-Raman spectroscopy

Micro-Raman spectra were recorded at room temperature using the 632.8 nm excitation wavelength. Fig. 5 shows the micro-Raman spectra observed in the range of 100-1500 cm^{-1} for several targeted regions of alkali-brick specimens. As can be seen in this figure, in most of targeted zones a strong band at around 456 cm^{-1} was detected and assigned to symmetric Si─O stretching vibration in the quartz structure [80]. The occurrence of a strong Raman band at 456 cm^{-1} proved the abundance of this mineral in the brick and its stability after alkali treatment, as already observed in X-ray diffractograms (see Fig. 3). Illite which was identified by XRD possessed an overlapping Raman band at around 465 cm^{-1} that were assigned to the symmetric Si─O bending vibrations (see [67] and references therein).

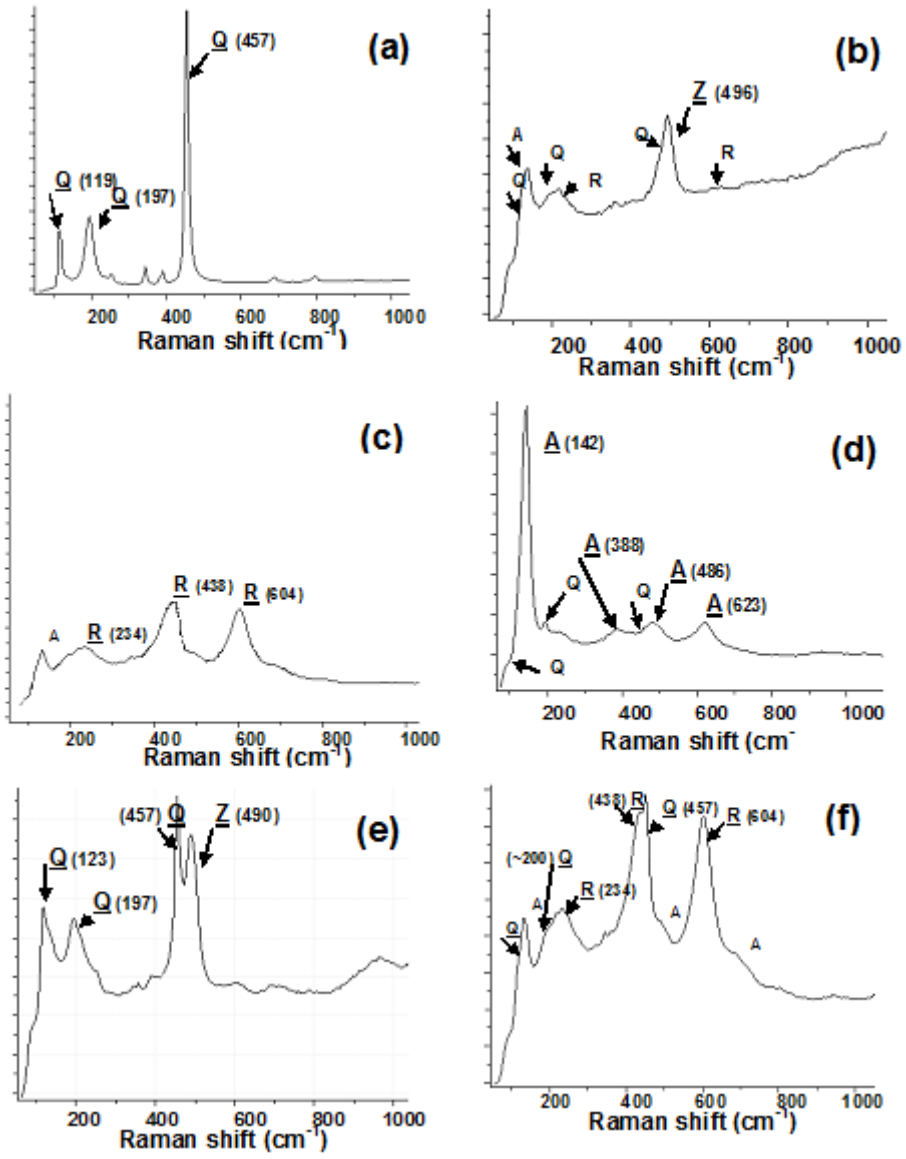

Figure 5: Micro-Raman spectra observed in the range of 100-1000 cm^{-1} for several (hazardously) targeted regions of alkali-brick specimens. Detection of nearly pure particles such as: quartz, rutile, and anatase in Figs. 5a, c, and d; a mixture of zeolite and quartz in Fig. 5e; a mixture of rutile, quartz and traces of anatase in Fig. 5f.

The Raman band related to illite intensifies the quartz band at 456 cm^{-1}, as pointed out previously [81]. Note that the spectrum in Fig. 5(a) is typical of SiO_2-rich particles, showing peaks at 120, 200, and 456 cm^{-1} which match well with the previously reported Raman data for quartz [82] (and consult ref. [83] and references therein). Moreover, the Raman spectra of some (hazardously) targeted regions display a relatively intense band at 490-496 cm^{-1}, confirming the dominant presence of NaP zeolite on brick surfaces, see Fig. 5b [61, 72, 84], although LTA zeolite (which was detected by XRD) cannot be excluded in the zeolitized

material. The frequency of the Raman 'NaP' band is related to the bending motion of the oxygen atom present in the T-O-T bonds (with T = Si; Al), and its value is found to be dependent upon the average T-O-T angle [10, 84]. The NaP-zeolite structure is indeed built-up of four-membered rings as the smallest building block [61, 84]. As a whole, micro-Raman findings (which showed mainly the existence of NaP and/or LTA in NaOH - treated brick) are consistent with ESEM/EDS data (see below in section 3.4). In other targeted specimens of NaOH - treated brick, micro-Raman investigations further revealed hazardously: (i) either nearly pure particles such as: quartz, rutile, and anatase (see Figs. 5a, c, and d); or (ii) different mixtures of minerals such as: zeolite + quartz (Fig. 5e), rutile + quartz + traces of anatase (Fig. 5f). Note that, all these brick minerals were identified by the XRD technique (as shown in Fig. 3) except for anatase because of its low amount in the brick. Note further that Micro-Raman assignments were made in the present study by taking into consideration previous works [85-87].

Combining the XRD, FTIR, and micro-Raman results, it was found that the alkali leaching of the brick at 90°C for six days induced the rearrangement of the alumino-silicate metakaolinite to generate LTA zeolite (as an intermediate and metastable compound) and NaP zeolite (as a thermodynamically more stable compound under our synthesis conditions.). To support these findings, the ESM/EDS technique was further applied here in the aim to survey the morphologies of the different zeolitic specimens formed in the alkali brick and to assess their elemental compositions.

3.4. ESEM/EDS analyses

Under weak alkali conditions (0.1mol.L^{-1} NaOH), no zeolite crystals were apparently formed in the reaction medium: the ESEM micrograph indeed shows brick surface being mostly composed of quartz crystals and amorphous phases/aggregates (Fig. 6a).

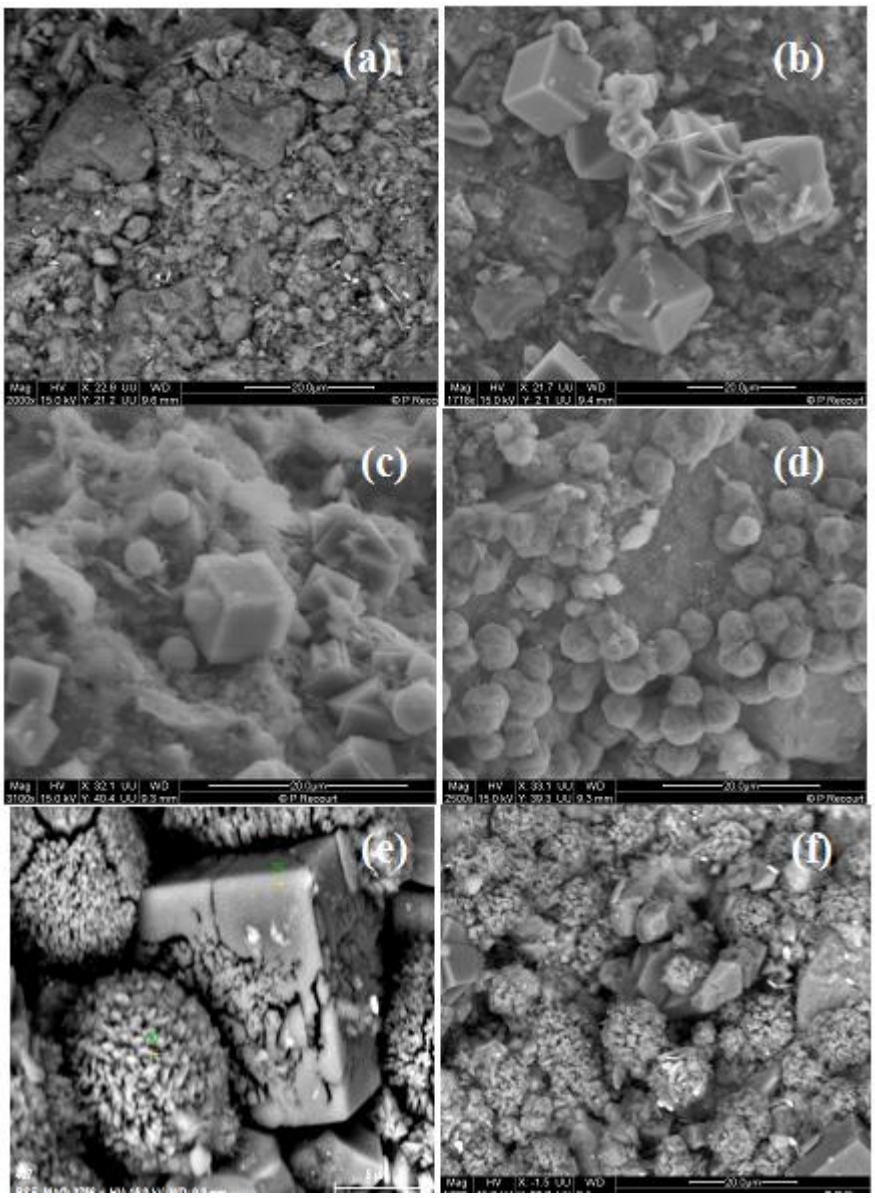

Figure 6: ESEM images of alkali brick samples synthesized at 90°C for 6 days (10 g of raw brick treated in 40 mL of NaOH solution): (a) in 0.1mol.L^{-1} NaOH; (b) 0.4mol.L^{-1} NaOH; (c) 0.6mol.L^{-1} NaOH; (d) 0.8 mol.L^{-1} NaOH; (e) crystalline transformation of the cubic crystals (as NaA zeolite) into spherical shape crystals (as NaP zeolite); (f) in 1.0-1.5mol.L^{-1} NaOH (spherical shape crystals having "cabbage" like structures).

It is worth to note that in the final mixture the liquid phase became cloudy, suggesting that an alumino-silicate gel was partly generated through the reaction between brick metakaolinite and sodium hydroxide [42, 63, 64, 88, 90-92]. Whereas, by increasing the reagent concentration to 0.4mol.L^{-1} NaOH, some zeolite nuclei grew on the surface of alumino-silicate particles in the form of cubic crystals (Fig. 6b). Along with increasing the reagent

concentration to 0.6mol.L^{-1} NaOH, the ESEM micrograph reveals the appearance of more cubic crystals at the brick grains and their averaged sizes ranged from 4 to 10 µm (see Fig. 6c): these well-developed cubic crystals are comparable of those observed previously by ESEM and attributed to the A-type zeolite [39, 93]. The same ESEM micrograph further shows the occurrence of spherical shape crystals in addition of cubic crystals, see Fig. 6c. These synthesized crystals which were identified as zeolite NaP, were found to be similar to those reported in the literature ([94-97].

After an alkaline treatment of the brick with a 0.8 mol.L^{-1} NaOH solution at 90°C for 6 days, the ESEM observations made on recovered brick pellets revealed predominantly spherical micro-particles with morphological and textural characteristics being comparable with those of NaP-zeolite, see Fig. 6d [94-97]. Each sphere was found to be isolated without aggregation and with averaged sizes varying from 3 to 7 µm. Interestingly, the nucleation in the synthesis of these spherical crystals took place at the surface of the cubic crystals, as illustrated in Fig. 6e, suggesting that the crystalline transformation of the cubic crystals (as NaA zeolite) should lead thermodynamically to a more stable alumino-silicate structure, as suggested previously [98, 99]. All these findings indicated clearly that, under such alkali conditions, the zeolitic transformation of brick metakaolinite into NaP zeolite took place completely, and during the course of this process NaA zeolite intervened in the reaction medium as a ‘metastable’ intermediate compound. These ESEM data are well consistent with XRD results reported in section 3.2.

Under stronger alkaline conditions (*i.e.* in 1.0-1.5 mol.L^{-1} NaOH), significant morphological transformations of the spherical shape crystals into more aggregated particles having “cabbage” like structures, occurred in the brick (Fig. 6f). This observation ascertains that the morphology of the NaP zeolite depended upon the experimental crystallization conditions (time) [76, 94, 100].

A simplified mechanism of metakaolinite zeolitization in the brick material could be proposed as follows. The hydroxide ions in alkali solution contributed to the dissolution of metakaolinite into silicate and aluminate ions. These ions condense to form Si─O─Al and Si─O─Si bonds, and to generate an intermediate alumino-silicate gel; subsequently, a slow condensation of this gel occurred in the reaction medium, leading to zeolite crystals. It is worth noting that during the course of the zeolitization process the substitution of Si^{4+} by Al^{3+}

ions in the framework building resulted in a "positive charge" deficit. This charge imbalance was offset by the incorporation of Na^+ ions into the zeolitic structure.

As brick zeolites belong to the GIS family, the chemical formula (based on the crystalline unit cell) should correspond to the crystalline phases:

$$(M)_{x/m}(Al)_x(Si)_{32-x}(O)_{32}.nH_2O(2)$$

where m is the valence of cations M; and n represents the number of water molecules per unit cell. In order to assess the averaged elemental composition of brick zeolites, detailed ESEM/EDS analyses of NaP and LTA crystals were carried out on brick surfaces. For that purpose, a series of cubic crystals (LTA) and spherical crystals (NaP) were targeted hazardously on several zeolitized -brick pellets. The averaged atomic percentages of Al, Si and Na were determined. We found the following structure formulae: $(Na)_{13.86\pm1.25}(?)_z(Al)_{16.43\pm0.99}(Si)_{15.89\pm0.98}(O)_{32}.nH_2O(3)$ ***for LTAcrystals***; $(Na)_{12.57\pm1.05}(?)_z(Al)_{14.92\pm1.14}(Si)_{15.58\pm1.45}(O)_{32}.nH_2O(4)$ ***for NaP crystals***.

The atomic deficit for sodium is represented by $(?)_z$ in formulae (3) and (4). In these formulae, The Si/Al atomic ratios are close enough to 1 (0.97 for LTA and 1.04 for NaP) and the stoichiometric coefficient x for aluminium range from 14.9 to 16.4 when compared to the general GIS structural formula (2). Also, we found an atomic deficit for sodium equal to: 13.86 ±1.25 and 12.57 ± 1.05, for LTA and NaP, respectively, instead of x ≈ 15-16. This Na deficit induces additional negative charges in the zeolite structures. To compensate this Na deficit, one ought to assume the involvement of other cations in NaP and LTA frameworks like: K^+, Ca^{2+} and/or Mg^{2+}, K^+, Ca^{2+} and Mg^{2+} ions that were well detected in the ESEM/EDS spectra of NaOH - treated brick samples (Fig. 7).

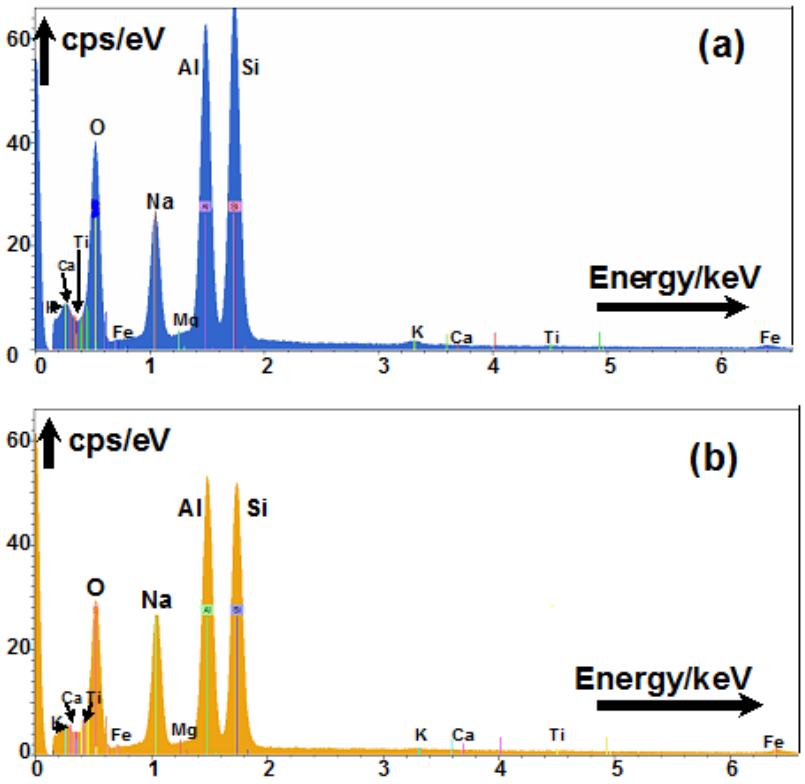

Figure 7: Typical ESEM/EDS spectra of cubic crystals (as NaA zeolite)__(a) and spherical shape crystals (as NaP zeolite)__(b), which were deposited on to (no-attacked) brick minerals (after alkali treatment of Bangui brick).

Such zeolitic structures composed of multiple cations could be compared to those proposed previously: for instance by Albert and his coworkers [101, 102]. However, the presence of impurities at the surfaces of these crystals could not be excluded, particularly, the existence of impurities containing iron and titanium as "Fe oxides" and "Ti dioxide", respectively, on crystals surfaces. These metals were detected by ESEM/EDS analyses (Fig. 7). It can be noticed that crystalline TiO_2 rutile was detected at brick surfaces by the XRD technique (see Fig. 3).

3.5. Ion-exchange properties of zeolitized brick towards cadmium(II) in fixed-bed column

The column tests packed with treated - brick pellets (with diameters varying from 0.7mm to 1.0mm) were conducted at given conditions of flow rate (2.5ml/min), bed depth (6.7-6.9 cm *i.e* 5.0029-5.0102 g of brick pellets), and fixed concentration of $Cd(NO_3)_2.4H_2O$ (54 mg of

cadmium per liter) in the influent at pH 4.91. The column performances were evaluated through the breakthrough curve of the continuous fixed-bed column, see Fig. 8.

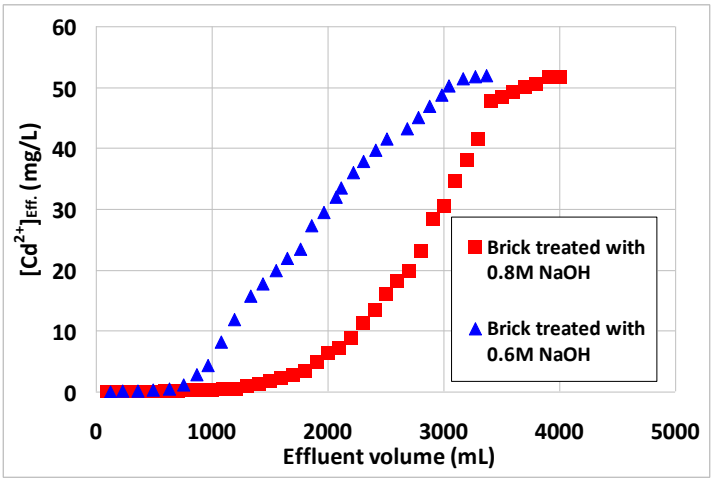

Figure 8: Breakthrough curves relative to the removal of Cd^{2+} ions in fixed-bed column by Bangui brick after alkali treatment at 90°C for 6 days: in 0.6mol.L^{-1} NaOH (▲); in 0.8mol.L^{-1} NaOH (■).

The breakthrough curve was commonly expressed as C_{eff} (or C_{eff}/C_o) against the contact time or volume of effluent, V_{eff} (where C_{eff} and C_o represent the oulet Cd(II) concentration and inlet Cd(II) concentration, respectively). The volumes of effluent collected at a time t and at the final time of the column experiment (t_{total}) are given by: $V_{eff} = F.t$ and $V_{eff}(final) = F.t_{total}$, where F is the volumetric flow rate (2.5 ml.min^{-1}). The total adsorbed metal ion (Q_{total}) by the column can be assessed by integrating the plot of adsorbed metal concentration, $C_{ads} = C_o - C_{eff}$, versus the flow time (t) by using the mathematical expression:

$$Q_{total} = \frac{F}{1000}\int_{t=0}^{t=t_{total}} (C_{ads}\,dt) \qquad (9)$$

The total amount of metal ion delivered to the system column (m_{total}) is obtained from eq.(10):

$$m_{total} = \frac{C_o.F.t_{Total}}{1000} \qquad (10)$$

The equilibrium metal ion uptake, q_{eq}, also known as the column maximum capacity is determined from the following equation:

$$q_{eq}(mg/g) = \frac{Q_{total}.}{X} \qquad (11)$$

where X is the mass of adsorbent (g) packed in the column. As for the removal efficiency Y (%), it was calculated from the equation:

$$Y(\%) = 100.. \frac{Q_{total}.}{m_{total}} \qquad (12)$$

Column parameters and breakthrough data were reported in Table 1.

Dynamic modeling of the breakthrough curve can be examined by using the Thomas model. The Thomas-model expression can be written as:

$$\frac{C_t}{C_o} = \frac{1}{1+\exp(k_{Th}/F)(q_{eq}.X - C_o.V_{eff.})} \qquad (13)$$

where k_{Th} (mL.min^{-1}.mg^{-1}) is the Thomas rate constant; q_{eq} (mg.g^{-1}) is the maximum adsorption capacity; X (g) is the total mass of the adsorbent loaded in the column adsorbent in the column; F (mL.min^{-1}) is the volumetric flow rate; and $V_{eff.}$ (mL) the volume of metal solution passed through the column. The linear form of the Thomas model is given by:

$$Ln(\frac{C_o}{C_t} - 1) = \frac{k_{Th}.q_{eq}.X}{F} - \frac{k_{Th}.C_o.V_{eff.}}{F} \qquad (14)$$

By fitting the experimental data to the model represented in linear form as: $Ln(\frac{C_o}{C_t} - 1)$ versus $V_{eff.}$ (effluent volume), Thomas model constant (k_{Th}) can be calculated from the slope of the plot and the equilibrium capacity (q_{eq}) can be calculated from the intercept of the plot. The values of the Thomas model were reported in Table 1.

Table 1: Column parameters and breakthrough data when using alkali brick pellets as ion exchanger/adsorbent.

Adsorbent: zeolitized brick prepared in 0.6M NaOH								
C_o *(mol/L)*	X *(g)*	F *(mL/min)*	m_{total} *(mg)*	t_b *(min)*	$t_{exh.}$ *(min)*	Q_{Total} *(mg)*	q_{eq} *(mg/g)*	Y *(%)*
$4.85x10^{-4}$	5.0029	2.5	180.95	302	1220	101.99	20.386	56.36
Thomas model data								
$k_{Th.}$ *(mL/(mg.min))*	q_{eq} *(mg/g)*	Y *(%)*	R^2					
0.08	20.320	56.18	0.995					

Adsorbent: zeolitized brick prepared in 0.8M NaOH								
C_o *(mol/L)*	X *(g)*	F *(mL/min)*	m_{total} *(mg)*	t_b *(min)*	$t_{exh.}$ *(min)*	Q_{Total} *(mg)*	q_{eq} *(mg/g)*	Y *(%)*
$4.85x10^{-4}$	5.0102	2.5	233.67	520	1520	161.08	32.151	68.94
Thomas model data								
$k_{Th.}$ *(mL/(mg.min))*	q_{eq} *(mg/g)*	Y *(%)*	R^2					
0.11	33.198	71.18	0.997					

The Thomas model's correlation coefficients are high (R^2 = 0.995-0.997), indicating that the model is able to describe the dynamic behavior of this column system.

Previously, we undertook in our lab the acid activation of Bangui brick followed by a deposition of ferrihydrite on to HCl-treated brick, and studied the adsorption capacity of the resulting material towards Cd^{2+} ions in fixed-bed column [48]. When compared the column data obtained with ferrihydrite-coated brick with those of zeolitized brick, one can notice that the total mass of adsorbate (Q_{total}) and the equilibrium metal ion uptake (q_{eq}) for zeolitized brick were greatly increased (see Tables 1 and 2), supporting the fact that the zeolitized brick can be considered as a better candidate than ferrihydrite-coated brick for the removal of cadmium(II) from aqueous solutions.

Table 2: Comparison of the maximum adsorption capacities of zeolitized-brick samples towards Cd(II) with those of natural zeolites, coated/modified zeolites, and coated sands documented in the literature.

Adsorbents	Adsorption capacity (mg/g)	References
(Algerian) Djebal Debbagh clay	18.51	Choumane and Benguella, 2013 [103]
Na-Montmorillonite	5.20	Abollino et al., 2003 [104]
Fly ash, treated	14.33	Chaiyasith et al., 2006 [105]
Manganese nodule residue	21.2	Rout et al., 2009[106]
Iron-coated silica	15.737(pH 5) ; 24.393(pH 7)	Waseem et al., 2011 [107]
Red mud	13.02	Gupta and Shama 2002 [108]
River bed sand	0.15	Sharma et al., 2007 [109]
Goethite-coated sand	0.05-0.20	Lai et al., 2002 [110]
Ukraine clinoptilolite	4.22	Sprynsky et al., 2006 [111]
Bigadic clinoptilolite	0.596	Turkman et al., 2004 [112]
Natural clinoptilolite	13.489-20.234	Gedik and Imamoglu, 2008 [113]
Sardinian natural zeolite	5.620-21.358	Cincotti et al., 2006 [114]
Na-modified ZRT	7.86-9.18	Barragan et al., 2017 [115]
Thiourea-modified ZRT	1.20-11.60	Barragan et al., 2017 [115]
Zeolite prepared from fly ash	26.246	Javadian et al., 2015 [116]
Acid-modified Transcarpathian clinoptilolite	7.41	Vasylechko et al., 2003 [117]
Natural and modified zeolites	23.6	Cukrovic et al., 1997 [118]
Na-A zeolite	60.758	Selim et al., 2017 [119]
Mn oxide coated zeolite	16	Irannadjad et al., 2016 [120]
Fe oxide coated zeolite	13	Irannadjad et al., 2016 [120]
Natural Jordanian zeolite	25.9	Taamneh et al., 2017 [121]
Ferrihydrite-coated brick	1.098	Allahdin et al., 2014 [47]
Zeolitized brick synthesized in 0.6M NaOH	20.386	This study
Zeolitized brick synthesized in 0.8M NaOH	32.151	This study

ZRT: zeolite-rich tuffs.

We afterwards compared the maximum adsorption capacities of zeolitized-brick samples towards Cd(II) (ranging from 20.32 to 33.20 mg/g) with those of natural zeolites and coated/modified zeolites documented in the literature (see Table 2). Except for Na-zeolite, the adsorption capacities of zeolitized brick pellets were, in all cases, found to be higher than those of natural zeolites and coated/modified zeolites (Table 2), thus confirming the importance of such a low-cost material (metakaolinite-containing brick) in the easy preparation of an efficient heavy-metals ion exchanger/adsorbent.

On the other hand, zeolitized brick can be considered roughly as a composite of sand and zeolite(s) in which sand represents more than 60% of the total brick mass. In this context, for comparison with the adsorption performances of zeolitized brick towards cadmium(II), the Cd(II)-adsorption capacities of some natural modified sands were also listed in Table 2. Likewise, the adsorption capacities of zeolitized brick pellets were found to be higher than those of coated sands, see Table 2.

4. CONCLUSION

The experimental results of this research indicated that the brick used was converted successfully to zeolitic products by treating it in atmospheric pressure with alkaline solution at 90°C. The atomic ratio Si/Al measured in these zeolitic products was close to 1, indicating the formation of "low silica" zeolites in Na-forms. These latter contained a maximum number of (sodic) negatively charged sites that were assumed to be potentially reactive with cationic heavy metals via electrostatic attraction forces existing at the brick-water interface.

Zeolitic framework building resulted in a "positive charge" deficit that was offset by the incorporation of Na^+ ions into the structure. The atomic ratio Na/Al in Na-zeolites was ≤ 1, suggesting that other cations such as K^+, Ca^{2+} and/or Mg^{2+} contributed as well to assure the electric charges balance in these zeolitic networks.

The feasibility of using alkali brick as a low-cost adsorbent in the elimination of a toxic heavy metal like cadmium(II) from aqueous solutions, was tested successfully in fixed-bed column. Total adsorbed metal ion (Q_{total}) and equilibrium metal ion uptake (q_{eq}) obtained for this material were comparable or better than those obtained with filters utilizing natural zeolites, coated/modified, and coated sand.

ACKNOWLEDGMENTS

This research was partly funded by the "Agence de l'Eau Artois-Picardie," and the "City Hall of Villeneuve d'Ascq". These investigations were undertaken successfully owing to the cooperation between the University of Lille1 (France) and the University of Bangui (Central African Republic). This collaboration (being still underway) and the Grant-in-Aid to Ms. N. Poumaye in for her Doctoral-Thesis preparation have been financially supported by the Embassy of France to Bangui. The authors gratefully thank David Dumoulin (Chemical Engineer) and Christine Grare and V. Alaimo (Chemical Technicians) for helping us usefully

in certain delicate chemical and/or analytical/spectroscopic studies, and Laurence Burylo (Chemical Technician) for recording X-ray diffractograms.

REFERENCES

1. World Health Organization (WHO) (2011). Cadmium in Drinking-water. WHO Guidelines for Drinking-water Quality (Geneva).
2. Ferraro, P.M., Costanzi, S., Naticchia, A., Sturniolo, A., Gambaro, G. Low level exposure to cadmium increases the risk of chronic kidney disease: analysis of the NHANES 1999-2006. BMC Publ. Health, 2010; 10 (304), 1-8. https://doi.org/10.1186/ 1471-2458-10-304.
3. Hyder, O., Chung, M., Cosgrove, D., Herman, J.M., Li, Z., Firoozmand, A., Gurakar, A., Koteish, A., Pawlik, T.M. Cadmium exposure and liver disease among US adults. J. Gastrointest. Surg., 2013; 17 (7): 1265-1273. https://doi.org/10.1007/s11605013-2210-9.
4. Kazantzis, G. Cadmium, osteoporosis and calcium metabolism. Biometals, 2004; 17 (5): 493-498. https://doi.org/10.1023/B: BIOM.0000045727.76054.f3.
5. Min, J.Y., Min, K.B. Blood cadmium levels and Alzheimer's disease mortality risk in older US adults. Environ Health., 2016;15(1): 1-6. https://doi: 10.1186/s12940-016-0155-7.
6. Tinkov, A.A., Filippini, T., Ajsuvakova, O.P., Aaseth, J., Gluhcheva, Y.G., Ivanova, J.M., Bjørklund, G., Skalnaya, M.G., Gatiatulina, E.R., Popova, E.V., Nemereshina, O.N., Vinceti, M., Skalny, A.V. The role of cadmium in obesity and diabetes. Sci. Total Environ., 2017; 601: 741-755. https://doi.org/10.1016/j.scitotenv.2017.05.224.
7. Tellez-Plaza, M., Navas-Acien, A., Menke, A., Crainiceanu, C.M., Pastor-Barriuso, R., Guallar, E. Cadmium exposure and all-cause and cardiovascular mortality in the US general population. Environ Health Perspect., 2012; 120(7): 1017–1022. https://doi.org/10.1289/ehp.1104352.
8. Hartwig, A. Cadmium and Cancer. In Cadmium: from Toxicity to Essentiality. Springer Netherlands, 2013: pp. 491-507. https://doi.org/10.1007/978-94-007-51798_15.
9. Townsend, R.P, Coker, E.N. in: E.M. Flanigen, P.A. Jacobs, J.C. Jansen, H. van Bekkum (Eds.), Introduction to Zeolite Science and Practice, Elsevier, Amsterdam, 2001: pp. 467-524.
10. Auerbach, S.M., Carrado, K.A., Dutta, P.K. Handbook of Zeolite Science and Technology. Marcel Dekker, Inc., New York, 2003.
11. Kim, J., Choi, M., Ryoo, R. Effect f mesoporosity against the deactivation of MFI zeolite catalyst during the methanol-to-hydrocarbon conversion process, J. catal., 2010; 269: 219-228.
12. Luo, J.-Y., Henry, H. Oh, C., Epling, W. Effect of C_3H_6 on selective catalytic reduction of NOx by NH_3 over a Cu/zeolite catalyst: a mechanistic study, Appl. Catal. B Environ., 2012; 123-124: 296-305.
13. Guo, Q., Fan, F., Pidko, E.A., Van Der Graaff, W.N.P., Feng, Z., Li, C., Hensen, E.J.M. Highly active and recyclable Sn-MWW zeolite catalyst for sugar conversion to methyl lactate and lactic acid, Inorg. Mater. Chem., 2013; 6(8): 1352-1356.
14. Teketel, S., Olsbye, U., Lillerud, K.P., Beato, P., Svelle, S. Co-conversion of methanol and light alkenes over acidic zeolite catalyst H-ZSM-22: simulated recycle of non-gasoline range products, Appl. Catal. A Gen., 2015; 494: 68-76.
15. Alotaibi, A., Hodgkiss, S., Kozhevnikova, E.F., Kozhevnikov, I.V. Selective alkylation of benzene by propane over bifunctional Pd-acid catalysts, Catalysts, 2017; 233: 1-10.
16. Moliner, M., Martinez, C., Corma, A. (2014). Synthesis strategies for preparing useful small pore zeolites and zeotypes for gas separations and catalysis, Chem. Mater., 2014; 26(1): 246-258.
17. Bhan, A., Nicholas Delgass, W. (2008). Propane aromatization over HZSM-5 and Ga/HZSM-5 catalysts, Catal. Rev., 2008; 50: 19-151.
18. Losch, P., Hoff, T.C., Kolb, J.F., Bernardon, C., Tessonnier, J.-P., Louis, B. Mesoporous ZSM-5 zeolites in acid catalysis: top-down vs. bottom-up approach, Catalysts, 2017; 225: 1-19.
19. Degnan, T.F., Chitnis, G.K., Schipper, P.H. History of ZSM-5 fluid catalytic cracking additive development at Mobil, Microporous and Mesoporous Materials, 2000; 35-36: 245-252.

20. Bjørgen, M., Joensen, F., Spangsberg Holm, M., Olsbye, U., Svelle, S. Methanol to gasoline over *zeolite* H-ZSM-5: Improved catalyst performance by treatment with NaOH. Applied Catalysis A*:* General, 2008; 345(1): 43-50.
21. Margeta, K., Zabukovec Logar, N., Siljeg, M., Farkas, A. Natural Zeolites in Water Treatment – How Effective is their Use. Chapter 5, licensee InTech, 2013: pp. 81-112. http://creativecommons.org/licenses/by/3.0. Chapter from the book Water Treatment Downloaded from: http://www.intechopen.com/books/water-treatment.
22. Yamane, I., Nakazawa, T. Development of zeolite for non-phosphated detergents in Japan. Pure & Appl. Chem., 1986; 58(10): 1397-1404.
23. Chopade, S.P., Nagarajan, K. Detergent Formulations: Ion Exchange. Michigan State University, USA, Academic Press, 2000: pp. 2560-2567.
24. Cinar, S., Beler-Baykal, B. Ion exchange with natural zeolites: an alternative for water softening? Water Science et Technology, 2005; 51: 71-77.
25. Lazar, L., Bandrabur, B., Tataru-Farmus, R.-E., Drobota, M., Stroe, S.-G., Gutt, G. Equilibrium performances of *CRYSTAL-RIGHT*^{TM} *CR100* zeolite used in water softening process. Environmental Engineering and Management Journal, 2015; 14(3): 541-549.
26. Alvarez-Ayuso, E., Garcia-Sanchez, A., Querol, X. Purification of metal electroplating wastewaters using zeolites. Water Research, 2003; 37(20): 4855-4862.
27. Erdem, E., Karapinar, N., Donat, R. The removal of heavy metal cations by natural zeolites. Journal of Colloid and Interface Science, 2004; 280: 309-314.
28. Wang, S., Peng, Y. Natural zeolites as effective adsorbents in water and wastewater treatment. Chemical Engineering Journal, 2010; 156: 11-24.
29. Shaheen, S.M., Derbalah, A.S., Moghanm, F.S. Removal of heavy metals from aqueous solution by zeolite in competitive sorption system. International Journal of Environmental Science and Development, 2012; 3(4): 362-367.
30. Cheng, T.W., Lee, M.L., Ko, M.S., Ueng, T.H., Yang, S.F. The heavy metal adsorption characteristics on metakaolin-based geopolymer. Applied Clay Science, 2012; 56: 90-96.
31. Nazarenko, O., Zarubina, R. Application of Sakhaptinsk zeolite for improving the quality of groundwater. Energy and Environmental Engineering, 2013; 1(2): 68-73.
32. Andrejkovicova, S., Sudagar, A., Rocha, J., Patinha, C., Hajjaji, W., Ferreira da Silva, E., Velosa, A., Rocha, F. The effect of natural zeolite on microstructure, mechanical and heavy metals adsorption properties of metakaolin based geopolymers. Applied Clay Science, 2016; 126: 141-152.
33. Jimenez-Castaneda, M.E., Medina, D.I. Use of surfactant-modified zeolites and clays for the removal of heavy metals from water. Water; 2017; 9, 235: 1-12. https://doi.org/10.3390/w9040235
34. Nery, J.G., Mascarenhas, Y.P., Cheetham, A.K. A study of the highly crystalline, low-silica, fully hydrated zeolite P ion exchanged with (Mn^{2+}, Cd^{2+}, Pb^{2+}, Sr^{2+}, Ba^{2+}) cations. Microporous and Mesoporous Materials, 2003; 57: 229-248.
35. Abdel Moamen, O.A., Ibrahim, H.A., Aldelmonem, N., Ismail, I.M. Thermodynamic analysis for the sorptive removal of cesium and strontium ions onto synthesized magnetic nano zeolite. Microporous and Mesoporous Materials, 2016; 223: 187-195.
36. Murat, M., Amokrane, A., Bastide, J.P., Montanaro, L. Synthesis of zeolites from thermally activated kaolinite. Some observations on nucleation and growth. Clay Minerals, 1992; 27: 119-130.
37. Akolekar, D., Chaffee, A., Howe, R.F. The transformation of kaolin to low-silica X zeolite. Zeolites, 1997; 19(5-6): 359-365.
38. Heller-Kallai, L., Lapides, I. Reactions of kaolinites and metakaolinites with NaOH—comparison of different samples (Part 1). Applied Clay Science, 2007; 35(1-2): 99-107.
39. Seliem, M.K., Komarneni, S. Equilibrium and kinetic studies for adsorption of iron from aqueous solution by synthetic Na-A zeolites: Statistical modeling and optimization. Microporous and Mesoporous Materials, 2016; 228: 266-274.
40. Temuujin, J., Okada, K., MacKenzie, K.J.D. Zeolite formation by hydrothermal treatment of waste solution from selectively leached kaolinite. Materials Letters, 2002; 52: 91-95.

41. Johnson, E.B.G., Arshad, S.E. Hydrothermally synthesized zeolites based on kaolinite: A review. Applied Clay Science, 2014; 97-98: 215-221.
42. Ayele, L., Pérez-Pariente, J., Chebude, Y., Diaz, I. Synthesis of zeolite A from Ethiopian kaolin. Microporous and Mesoporous Materials, 2015; 215: 29-36.
43. Zayed, A.M., Selim, A.Q., Mohamed, E.A., Abdel Wahed, M.S.M., Seliem, M.K., Sillanpaa, M. Adsorption characteristics of Na-A zeolites synthesized from Egyptian kaolinite for manganese in aqueous solutions: Response surface modelling and optimization. Applied Clay Science, 2017; 140: 17-24.
44. Dehou, S.C., Mabingui, J., Lesven, L., Wartel, M., Boughriet, A. Improvement of Fe(II)-adsorption capacity of FeOOH-coated brick in solutions, and kinetics aspects. J. Water Resourc. Protection, 2012; 4: 464-473.
45. Dehou, S.C., Wartel, M., Recourt, P., Revel, B., Mabingui, J., Montiel, A., Boughriet, A. Physicochemical, crystalline and morphological characteristics of bricks used for ground waters purification in Bangui region (Central African Republic). Appl. Clay Sci., 2012; 59-60:69-75.
46. Allahdin, O., Dehou, S.C., Wartel, M., Recourt, P., Trentesaux, M., Mabingui, J., Boughriet, A. Performance of FeOOH-brick based composite for Fe(II) removal from water in fixed bed column and mechanistic aspects. Chem. Eng. Res. and Design, 2013; 91: 2732-2742.
47. Allahdin, O., Wartel, M., Recourt, P., Revel, B., Ouddane, B., Billon, G., Mabingui, J., Boughriet, A. Adsorption capacity of iron oxyhydroxide-coated brick for cationic metals and nature of ion surface interactions. Appl. Clay Sci., 2014; 90:141–149.
48. Allahdin, O., Wartel, M., Mabingui, J., A. Boughriet, A. Kinetics of divalent Metals (Cd^{2+}, Cu^{2+}, Pb^{2+}, Zn^{2+}) adsorption onto a modified brick. Am. Chem. Sci. J., 2014; 4(5): 687-705.
49. Allahdin, O., Wartel, M., Mabingui, J., Revel, B., Nuns, N., Boughriet, A. Surface characteristics of the iron-oxyhydroxide layer formed during brick coatings by ESEM/EDS, ^{23}Na and ^{1}H MAS NMR, and ToF-SIMS. Mater. Chem. Phys., 2015; 165: 215-226.
50. Allahdin, O., Wartel, M., Mabingui, J., Boughriet, A. Implication of electrostatic forces on the adsorption capacity of a modified brick for the removal of divalent cations from water. Am. J. Anal. Chem., 2015; 6: 11-25.
51. Allahdin, O., Bagoua, B., Wartel, M., Mabingui, J., Boughriet, A. Effects of chemical activation on surface sites of the brick: pH-dependence on metal adsorption. International J. New Technol. Res., 2016; 2(1): 22-31.
52. Labidi, N.S. Removal of mercury from aqueous solutions by waste brick. Inter. J. Environ. Res., 2008; 2(3): 275-278.
53. Witharana, A., Jayaweera, M., Manatunge, J. Zinc adsorption by low cost sorbent materials: Clay title, brick, sawdust and rice husk. International Conference on Sustainable Built Environment (ICSBE-2010), Kandy, 13-14 Decembre 2010: pp. 21-28.
54. Gandhi, N., Sirisha, D., Chandra Sekhar, K.D. Adsorption studies of chromium by using low cost adsorbents. Our Nature, 2013; 11(1): 11-16.
55. Hemalatha, P.V., Prasada Rao, P.V.V. Adsorption batch studies on calcined brick powder in removing chromium and nickel ions. Inter. J. Adv. Res. Chem. Sci., 2014; 1(6): 14-21.
56. Krishna, R.H., Swamy, A.V.V.S. Physico-chemical key parameters, Langmuir and Freundlich isotherm and Lagergren rate constant studies on the removal of calcined brick. Inter. J. Eng. Res. Dev., 2012; 4(1): 29-38.
57. M. Visa, M. Synthesis and characterization of new zeolite materials obtained from fly ash for heavy metals removal in advanced wastewater treatment. Powder Technology, 2016; 294: 338-347.
58. Roozeboom, F., Robson, H.E., Chan, S.S. Laser Raman study on the crystallization of zeolites A, X and Y. Zeolites, 1983; 3: 321-328.
59. Dutta, P.K., Shieh, D.C. Influence of alkali chlorides on distribution of aqueous base solubilized silicate species. Zeolites, 1985; 5: 135-138.
60. G. Engelhardt, G., B. Fahlke, B., M. Mägi, M., E. Lippmaa, E. High-resolution solid - state ^{29}Si and ^{27}Al n.m.r. of aluminosilicate intermediates in the synthesis of zeolite A. Part II. Zeolites, 1985; 5: 49-52.
61. Twu, J., Dutta, P.K., Kresge, C.T. Raman spectroscopic studies of the synthesis of faujasitic zeolites: Comparison of two silica sources. Zeolites, 1991; 11: 672-679.
62. Li, P., Ding, T., Liu, L., Xiong, G. Investigation on phase transformation mechanism of zeolite NaY under alkaline hydrothermal conditions. Materials Characterization, 2013; 86: 221-231.

63. Chen, T.-H, Houthoofd, K., Grobet, P.J. Toward the aluminium coordination in dealuminated mordenite and amorphous silica-alumina: A high resolution 27Al MAS and MQ MAS NMR study. Microporous and Mesoporous Materials, 2005; 86: 31-37.
64. Rees, L.V.C., Chandrasekhar, S. Formation of zeolite from the system Na_2O-Al_2O_3-SiO_2-H_2O in alkaline medium (pH<10). Zeolites, 1993; 13: 524-533.
65. Treacy, M.M.J., Higgins, J.B. Collection of Simulated XRD Powder Patterns for Zeolites (4th Revised Edition), Elsevier, New York, 2001: pp. 174-175 and 212-215.
66. Hansen, S., Hakansson, U., Landa-Canovas, A.R., Fälth, L. On the crystal chemistry of NaP zeolites. Zeolites, 1993; 13: 276-280.
67. Liu, W. Modeling description and spectroscopic evidence of surface acid-base properties of natural illites. Wat. Res., 2001; 35(17): 4111-4125.
68. Jiang, T., Li, G., Qiu, G., Fan, X., Huang, Z. Thermal activation and alkali dissolution of silicon from illite. Applied Clay Science, 2008; 40: 81-89.
69. Ali, I.O., El-Sheikh, S.M., Salama, T.M., Bakr, M.F., Fodial, M.H. Controllable synthesis of NaP zeolite and its application in calcium adsorption. Science China Materials, 2015 58(8): 621-633.
70. Sanchez-Hernandez, R., Lopez-Delgado, A., Padilla, I., Galindo, R., Lopez-Andrés, S. One-step synthesis of NaP1, SOD and ANA from a hazardous aluminum solid waste. Microporous and Mesoporous Materials, 2016; 226: 267-277.
71. Gil, B., Roth, W.J., Makowski, W., Marszalek, B., Majda, D., Olejniczak, Z., Michorczyk, P. Facile evaluation of the crystallization and quality of the transient layered zeolite MCM-56 by infrared spectroscopy. Catalysis Today, 2015; 243: 39-45.
72. Kröl, M., Mozgawa, W., Morawska, J., Pichor, W. Spectroscopic investigation of hydrothermally synthesized zeolites from expanded perlite. Microporous and Mesoporous Materials, 2014; 196: 216-222.
73. Wang, Y., Lin, F. Synthesis of high capacity cation exchangers from a low-grade Chinese natural zeolite. Journal of Hazardous Materials, 2009; 166: 1014-1019.
74. Prokof'ev, V.Y., Gordina, N.E., Khramtsova, A.P., Konstantinova, E.M., Cherednikova, D.S. Synthesis of binder-free granulated low-modular zeolites using ultrasound. Microporous and Mesoporous Materials, 2017; 242: 63-73.
75. Sanchez-Hernandez, R., Padilla, I., Lopez-Andrés, S., Lopez-Delgado, A. Eco-friendly bench-scale zeolitization of an Al-containing waste into gismondine-type zeolite under effluent recycling. Journal of Cleaner Production, 2017; 161: 792-802.
76. Huo, Z., Xu, X., Lü, Z., Song, J., He, M., Li, Z., Wang, Q., Yan, L. Synthesis of zeolite NaP with controllable morphologies. Microporous and Mesoporous Materials, 2012; 158: 137-140.
77. Gordina, N.E., Prokof'ev, V.Y., Kul'pina, Y.N., Petuhova, N.V., Gazahova, S.I., Hmylova, O.E. Effect of ultrasound on the synthesis of low-modulus zeolites from a metakaolin. Ultrasonics Sonochemistry, 2016; 33: 210-219.
78. de Andrade Bessa, R., de Sousa Costa, L., Pinto Oliveira, C., Bohn, F., do Nascimento, R.F., Sasaki, J.M., Loiola, A.R. Kaolin-based magnetic zeolites A and P as water softeners. Microporous and Mesoporous Materials, 2017; 245: 64-72.
79. Mullins, L.J., Tiffert, T., Vassort, G., Whittembury, J. The effects of internal Na^+ and H^+ and of external Ca^{2+} and membrane potential on Ca entry in squid axons. J. Physiol., 1983; 338: 295-319.
80. Yin, Y., Yin, J., Zhang, W., Tian, H., Hu, Z., Ruan, M., Xu, H., Liu, L., Yan, X., Chen, D. FT-IR and micro-Raman spectroscopic characterization of minerals in high-calcium coal ashes. Journal of the Energy Institute, 2017; xxx: 1-8. *In press.*
81. Caner, E., Güney, B.A. Characterization of cramic ware fragments from aizanoi-Turkey by microRaman, XRPD and SEM-EDX spectroscopy. Spectrochimica Acta Part A: Molecular and Biomolecular Spectroscopy, 2017; 177: 135-139.
82. Fridrichova, J., Bacik, P., Illasova, L., Kozakova, P., Skoda, R., Pulisova, Z., Fiala, A. Raman and optical spectroscopic investigation of gem-quality smoky quartz crystals. Vibrational Spectroscopy, 2016; 85: 71-78.
83. Reinosa, J.J., del Campo, A., Fernandez, J.F. Indirect measurement of stress distribution in quartz particles embedded in a glass matrix by using confocal Raman microscopy. Ceramics International, 2015; 41: 13598-13606.

84. Dutta, P.K., Shieh, D.C., Puri, M. Correlation of framework Raman bands of zeolites with structure. Zeolites, 1988; 8: 306-309.
85. Municchia, A.C., Micheli, M., RICCI, M.A., Toledo, M., Bellatreccia, F., Lo Mastro, S., A. Sodo, A. Raman, SEM-EDS and XRPD investigations on pre-Colombian Central America 'estucado' pottery. Spectrochimica Acta Part A: Molecular and Biomolecular Spectroscopy, 2016; 156: 47-53.
86. Selman, A.M., Husham, M. calcinations induced transformation of TiO_2 nanostructures and fabricated a schottky diode as humidity sensor based on rutile phase. Sensing and Bio-Sensing Research, 2016; 11: 8-13.
87. Wan, G., Wang, S., Li, L., Mu, G., Yin, X., Zhang, X., Tang, Y., Yi, L. Photocarrier dynamic measurement of rutile TiO_2 films prepared by RF magnetron reactive sputtering. Journal of Alloys and Compounds, 2017; 701: 549-553.
88. Glid, M., Sobrados, I., Ben Rhaiem, H., Sanz, J., Ben Haj Amara, A. Alkaline activation of metakaolinite-silica mixtures: Role of dissolved silica concentration on the formation of geopolymers. Ceramics International, 2017; 43: 12641-12650.
89. Lippmaa, E., Mägi, M., Samoson, A., Tarmak, M., Engelhardt, G. Investigation of the structure of zeolites by solid-state high-resolution 29Si NMR spectroscopy. J. Am. Chem. Soc., 1981; 103: 4992–4996.
90. Zibouche, F., Kerdjoudj, H., d'Espinose de Lacaillerie, J.-B., Van Damme, H. Geopolymers from Algerian metakaolin. Influence of secondary minerals. Applied Clay Science, 2009; 43: 453–458.
91. Wang, H., Li, H., Yan, F. Synthesis and mechanical properties of metakaolinite-based geopolymer. Colloids and Surfaces A: Physicochem. Eng. Aspects, 2005; 268: 1-6.
92. Yao, X., Zhang, Z., Zhu, H., Chen, Y. Geopolymerization process of alkali-metakaolinite characterized by isothermal calorimetry. Thermochimica Acta, 2009; 493: 49-54.
93. S. Tontisirin, S. Synthesis and characterization of co-crystalline zeolite composite of LSX/A. Microporous and Mesoporous Materials, 2017; 239: 123-129.
94. Zubowa, H.-L., Kosslick, H., Müller, D., Richter, M., Wilde, L., Fricke, R. Crystallization of phase-pure zeolite NaP from MCM-22-type gel compositions under microwave radiation. Microporous and Mesoporous Materials, 2008; 109: 542–548.
95. Sathupunya, M., Gulari, E., Wongkasemjit, S. ANA and GIS zeolite synthesis directly from alumatrane and silatrane by sol-gel process and microwave technique. Journal of the European Ceramic Society, 2002; 22: 2305–2314
96. Khabuanchalad, S., Khemthong, P., Prayoonpokarach, S., Wittayakun, J. Transformation of zeolite NaY synthesized from rice husk silica to NaP during hydrothermal synthesis. Suranaree J. Sc. Technol., 2008; 15: 225-231.
97. Behin, J., Kazemian, H., Rohani, S. Sonochemical synthesis of zeolite NaP from clinoptilolite. Ultrasonics Sonochemistry, 2016; 28: 400-408.
98. Torres Sanchez, R.M., Basaldella, E.I., Tara, J.C., Zeolites surface reactions pointed out by charge parameters. Materials Letters, 2001; 50: 138-144.
99. Bohra, S., Kundu, D., Kanti Naskar, M. Synthesis of cashew nut-like zeolite NaP powders using agro-waste material as silica source. Materials Letters, 2013; 106: 182-185.
100. Vereshchagina, T.A., Vereshchagin, S.N., Shishkina, N.N., Mikhaylova, A.A., Solovyov, L.A., Anshits, A.G. One-step fabrication of hollow aluminosilicate microspheres with composite zeolite/glass crystalline shell. Microporous and Mesoporous Materials, 2013; 169: 207-211.
101. Albert, B.R., Cheetham, A.K., Stuart, J.A., Adams, C.J. Investigations on P zeolites: synthesis, characterisation, and structure of highly crystalline low-silica NaP. Microporous and Mesoporous Materials, 1998; 21: 133–142.
102. Albert, B.R., Cheetham, A.K. A synchrotron X-ray powder diffraction study of highly crystalline low-silica zeolite P during Na-Ca ion exchange. Microporous and Mesoporous Materials, 2000; 34: 207–211.
103. Choumane, F.Z., Benguella, B. Effects of Algerian clays properties on the adsorption of Cd(II). Journal of Environmentally Friendly Processes; ISSN: 2328-1383, 2013; 1(2): 10-21.
104. Abollino, O., Aceto, M., Malandrino, M., Sarzanini, C., Mentasti, E. Adsorption of heavy metals on Na-montmorillonite : effect of pH and organic substances. Water Res., 2003; 37: 1619-1627.
105. Chaiyasith, S., Chaiyasith, P., Septhum, C. Removal of cadmium and nickel from aqueous solution by adsorption onto treated fly ash from Thailand, Int. J. Sci. Technol., 2006; 11(2): 13-20.

106. Rout, K., Mohapatra, M., Mohapatra, B.K., Anand, S. Pb(II), Cd(II) and Zn(II) adsorption on low grade manganese ore. International Journal of Engineering, Science and Technology, 2009; 1(1): 106-122.
107. Waseem, M., Mustafa, S., Naeem, A., Koper, G.J.M., Shah, K.H. Cd^{2+} sorption characteristics of iron coated silica. Desalination, 2011; 277: 221-226.
108. Gupta, V.K., Sharma, S. Removal of cadmium and zinc from aqueous solutions using red mud. Environ. Sci. Technol., 2002; 36: 3612-3617.
109. Sharma, Y.C., Kaul, S.N., Weng, C.H. Adsorptive separation of cadmium from aqueous solutions and wastewaters by riverbed sand. Environmental Pollution, 2007; 150: 251-257.
110. Lai, C.-H., Chen, C.-Y., Wei, B.-L., Yeh, S.-H. Cadmium adsorption on goethite-coated sand in the presence of humic acid. Water Research, 2002; 36: 4943–4950.
111. Sprynskyy, M., Buszewski, B., Terzyk, A.P., Namiesnik, J. Study of the selection mechanism of heavy metal (Pb^{2+}, Cu^{2+}, Ni^{2+}, and Cd^{2+}) adsorption on clinoptilolite. J. Colloid Interface Sci., 2006; 304: 21-28.
112. Turkman, A.E., Aslan, S., Ege, I. Treatment of metal containing wastewaters by natural zeolites. Fresenius Environ. Bull., 2004; 13: 574–580.
113. Gedik, K., Imamoglu, I. Affinity of clinoptilolite-based zeolites towards removal of Cd from aqueous solutions. Sep. Sci. Technol., 2008; 43(5): 1191–1207.
114. Cincotti, A., Mameli, A., Locci, A.M., Orrú, R., Cao, G. Heavy metal uptake by Sardinian natural zeolites: Experiment and modeling. Ind. Eng. Chem. Res., 2006; 45(3): 1074–1084.
115. Barragán P., Guadalupe Macedo, M., Olguín, M.T. Cadmium sorption by sodium and thiourea-modified zeolite-rich tuffs. J. Environ. Sci., 2017; 52: 39-48.
116. Javadian, H., Ghorbani, F., Tayebi, H., Hosseini Asl , S.M. Study of the adsorption of Cd (II) from aqueous solution using zeolite-based geopolymer, synthesized from coal fly ash; kinetic, isotherm and thermodynamic studies. Arabian Journal of Chemistry, 2015; 8: 837–849.
117. Vasylechko, V.O., Gryshchouk, G.V., Kuz'ma, Y.B., Zakordonskiy, V.P., Vasylechko, L.O., Lebedynets, L.O., Kalytovs'ka, M.B. Adsorption of cadmium on acid-modified Transcarpathian clinoptilolite. Microporous and Mesoporous Materials, 2003; 60(1-3): 183-196.
118. Curkovic, L., Cerjan-Stefanovic, S., Filipan, T. Metal ion exchange by natural and modified zeolites. Water Research, 1997; 31(6): 1379-1382.
119. Selim, M.M., El-Mekkawi, D.M., Aboelenin, R.M.M., Sayed Ahmed, S.A., Mohamed, G.M. Preparation and characterization of Na-A zeolite from aluminum scrub and commercial sodium silicate for the removal of Cd^{2+} from water. Journal of the Association of Arab Universities for Basic and Applied Sciences, 2017; 24: 19-25.
120. Irannadjad, M., Kamran Haghighi, H., Soleimanipour, M. Adsorption of Zn2+, Cd2+ and Cu2+ on zeolites coated by manganese and iron oxides. Physicochem. Probl. Miner. Process., 2016; 52(2): 894−908.
121. Taamneh, Y., Sharadqah, S. The removal of heavy metals from aqueous solution using natural Jordanian zeolite. Applied Water Science, 2017; 7(4): 2021-2028.